ELSEVIER

Contents lists available at ScienceDirect

Scripta Materialia

journal homepage: www.elsevier.com/locate/scriptamat



On temperature and strain-rate dependence of flow serration in HfNbTaTiZr high-entropy alloy



Shuying Chen^a, Weidong Li^{b,c,*}, Fanchao Meng^a, Yang Tong^a, Hua Zhang^a, Ko-Kai Tseng^d, Jien-Wei Yeh^d, Yang Ren^e, Fei Xu^f, Zhenggang Wu^{g,*}, Peter K. Liaw^{b,*}

- ^a Institute for Advanced Studies in Precision Materials, Yantai University, Yantai, Shandong, 264005, China
- ^b Department of Materials Science and Engineering, The University of Tennessee, Knoxville, TN, 37996, USA
- c Blue Origin, Kent, WA, 98032, USA
- d High Entropy Materials Center, Department of Materials Science and Engineering, National Tsing Hua University, Hsinchu, 30013, Taiwan
- ^e X-ray Science Division, Argonne National Laboratory, Argonne, IL, 60439, USA
- f Ansys Inc., Austin, TX, 78746, USA
- ⁸ College of Materials Science and Engineering, Hunan Province Key Laboratory for Spray Deposition Technology and Application, Hunan University, Changsha, 410082, China

ARTICLE INFO

Article history: Received 4 March 2021 Accepted 5 April 2021 Available online 16 April 2021

Keywords: High-entropy alloys Serrated flow Portevin-Le Chatelier effect Dynamic strain aging Theoretical modeling

ABSTRACT

Plastic instability manifested as the serrated flow on stress-strain curves of metal alloys is generally detrimental to their processing and manufacturing. The flow serration in the HfNbTaTiZr alloy is reported in the present work and its dependence on temperatures (573-823K) and strain rates (5 \times 10⁻⁵ s⁻¹- 1 \times 10⁻³ s⁻¹) is investigated with experiments. The notable transition of the onset strain of the serrated flow from a declining (normal behavior) to rising (inverse behavior) trend with increasing temperature at applied strain rates is modeled successfully with a theoretical framework. The success of the model in predicting the onset strain as a function of temperature and strain rate represents a possibility of theoretically constructing a process window for the alloy under examination and beyond.

© 2021 Acta Materialia Inc. Published by Elsevier Ltd. All rights reserved.

The Portevin-Le Chatelier (PLC) effect, a plastic instability phenomenon manifested as serrated flow on stress-strain curves, has been observed in many alloy systems in given ranges of temperature and strain rate [1–4]. In general, the flow serration in metal alloys is mechanistically attributed to dynamic strain aging (DSA), a micro-mechanism involving the interaction between mobile dislocations and diffusing solute atoms or deformation twins [5]. Flow serration is also noted in some of recently emerged high-entropy alloys (HEAs) [6,7] the Al_xCoCrCu_xFeNi [8–12], CrMnFeCoNi [13], and MoNbTaTiV refractory alloys [14]. Despite the resemblance in the stress-strain curve appearance, the underlying DSA process responsible for serrated flow in conventional dilute alloys and concentrated HEAs is supposedly distinct, considering that all element species in the latter may be deemed as solutes.

Historically, the investigation of DSA mechanisms in conventional dilute alloys has drawn plentiful attention and is proven useful to engineering applications of corresponding alloys. By and large, understanding the DSA mechanism in detail enables the

E-mail addresses: wli20@utk.edu (W. Li), zwu9@hnu.edu.cn (Z. Wu), pliaw@utk.edu (P.K. Liaw).

identification of the solute element accountable for serrated flow in various test conditions, and thus, facilitates the development of countermeasures to mitigate property deterioration during manufacturing or processing [15,16]. Undoubtedly, understanding serrated flows phenomenologically and theoretically in HEAs is equivalently critical. On one hand, it is constructive to fundamental understandings of the solute-dislocation interplay in concentrated HEAs, revealing its linkage with macroscopic mechanical responses. On the other hand, it could positively promote the engineering adoption of this family of alloys. Following our previous work [17], we here continue to use the refractory HfNbTaTiZr with a bodycentered-cubic (BCC) structure as a prototype to study its serration behavior under tension in a range of applied temperatures and strain rates. Emphasis is presently placed on the theoretical prediction of the onset strain of the serrated flow as a function of temperature and strain rate.

The fabrication and processing of the HfNbTaTiZr alloy used for this study followed the steps outlined in Ref. [17]. The mechanical properties were determined under uniaxial tensile tests in a Material Test System (MTS) servohydraulic machine at three strain rates of $1\times10^{-3}~s^{-1}$, $2\times10^{-4}~s^{-1}$ and $5\times10^{-5}~s^{-1}$ and temperatures from 573 K to 873 K, under displacement control. At least two tests were repeated for each condition. Synchrotron diffractions were

^{*} Corresponding authors:

S. Chen, W. Li, F. Meng et al. Scripta Materialia 200 (2021) 113919

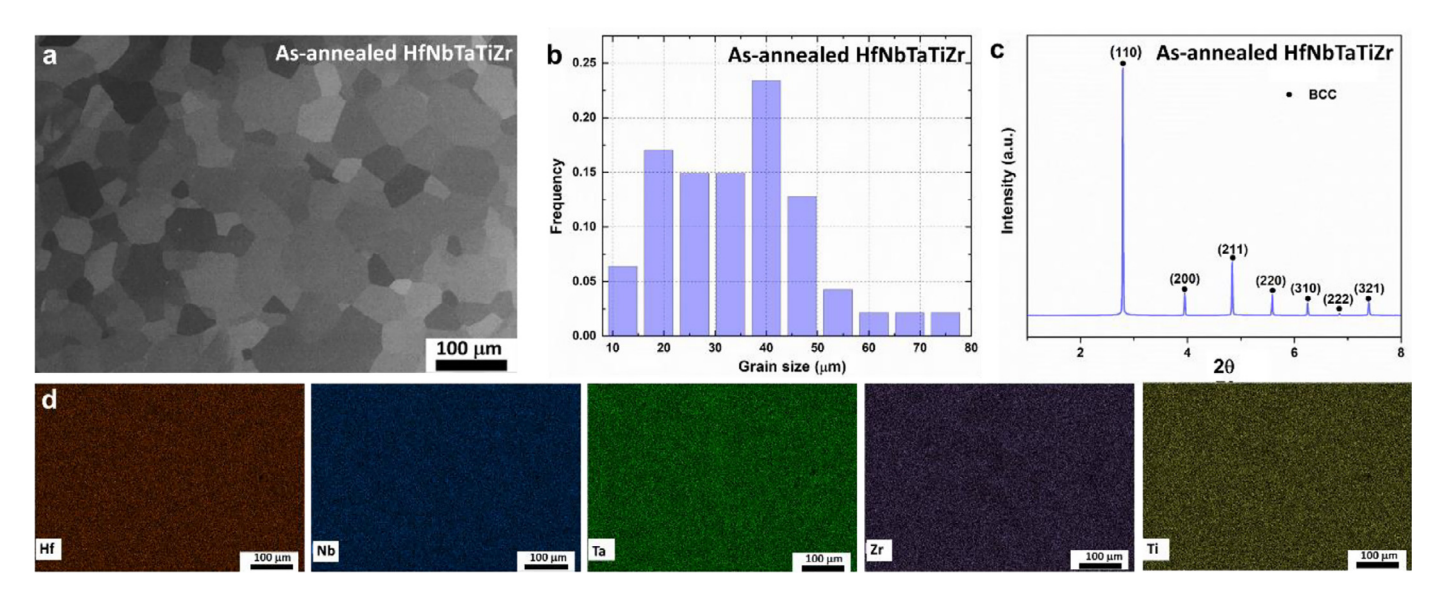


Fig. 1. Microstructural information of the as-annealed HfNbTaTiZr alloy. (a) SEM backscattered electron (BSE) micrograph. (b) Grain-size distribution. (c) X-ray diffraction. (d) SEM energy dispersive spectroscopy (EDS) mappings.

conducted on the 11ID-C beamline (beam energy of 115.27 keV), at the Advanced Photon Source (APS) of Argonne National Laboratory. Microstructural examinations were achieved by scanning electron microscopy (SEM) of LEO 1525 at 30 keV.

Following cold-rolling and annealing, the microstructure of the HfNbTaTiZr alloy consists of equiaxed grains with the average grain size of 35-45 μ m, as revealed in Fig. 1a-b. X-ray diffraction in Fig. 1c confirms its BCC structure. The elemental maps in Fig. 1d, imaged by energy dispersive spectroscopy (EDS) equipped with SEM, evidences the uniform distribution of compositional elements across the heat-treated alloys.

The mechanical responses of the alloy under uniaxial tensions at temperatures ranging from 573 K to 823 K and strain rates from $5\times 10^{-5}~\text{s}^{-1}$ to $1\times 10^{-3}~\text{s}^{-1}$ are shown Fig. 2a-c. The dependence of yield strength (YS) and ultimate tensile strength (UTS) on temperature and strain rate is summarized in Fig. 2d. In respect to temperature effect, the samples tested at $5\times 10^{-5}~\text{s}^{-1}$ and $2\times 10^{-4}~\text{s}^{-1}$ exhibit like trends, that is, YS and UTS first decrease as the temperature ramps from 573 K to 723 K, but reverts to an upturn at 773 K. On the other hand, the samples at $1\times 10^{-3}~\text{s}^{-1}$ manifest a somewhat contrasting trend, that is, both YS and UTS first rise (slightly though) and then drop as the temperature varies from 673 K to 773 K. The influence of strain rate on the uniaxial mechanical behavior of the alloy is classical, *i.e.*, the material hardens slightly as the strain rate increases.

Moreover, plastic flow in the full range of temperatures and strain rates are observed to transition from being stable and smooth to be unstable and serrated when some critical strain are passed. Usually, the observed PLC characteristics were classified as Type A, B, and C depending on the imposed temperature, strain rate, strain hardening and the material state (cold-rolled or annealed). At all applied strain rates, serrated flow exhibits a tendency of shifting from Type A to Type C as testing temperature increases, as illustrated in Fig. 2a-c.

In conventional dilute alloys, flow serration is generally associated with the very low or even negative strain rate sensitivity of the flow stress. To appraise its applicability in HEAs, the strain rate sensitivity (SRS) of the present alloy is evaluated with [18]

$$m = \frac{\log(\sigma_2/\sigma_1)}{\log(\dot{\varepsilon}_2/\dot{\varepsilon}_1)} \tag{1}$$

where σ_1 and σ_2 are the flow stresses at the corresponding strain rates of $\dot{\varepsilon}_1 = 5 \times 10^{-5} \ s^{-1}$ and $\dot{\varepsilon}_2 = 2 \times 10^{-4} \ s^{-1}$, respectively. With the aid of Eq. (1), we calculate the strain rate sensitivity, m, of the alloy at three distinct temperature (i.e., 573 K, 673 K, and 773 K). For each temperature, the flow stresses at two different strain levels, i.e., 0.07 and 0.09, are read from the DSA regime of the stress-strain curves for calculation. The calculation results are plotted in Fig. 3. It is found that the strain rate sensitivity at all three temperatures are negative, with strain level having minimal influence. This observation is essentially consistent with what has been reported in conventional alloys [18].

Of all characteristics in Fig. 2, the most striking one is, however, that flow serration in the HfNbTaTiZr alloy commences at varying strain levels depending on temperature and strain rate. From a processing standpoint, it is crucial to know the onset strains of serrated flows in various conditions, as it can aid in defining the process window within which plastic instability may be safely circumvented, mitigated, or taken advantage of. Defining such a process window in a wide range of temperatures and strain rates with the experimental methodology is surely costly, time-consuming, and less expandable. In consideration of this shortage in experiments, we attempt to use theoretical analysis to predict the temperature and strain rate dependence of the onset strain of the serrated flow in the HfNbTaTiZr alloy. The theoretical framework outlined below is anticipated to be extendable to other alloy systems with the same problem.

As a first step, the onset strain, ε_c , in all testing conditions are identified, marked with red dots in Fig. 2, complied in Table 1, and plotted in Fig. 4 as solid symbols. From Fig. 4, it is seen that at three strain rates, ε_c invariably decreases with increasing temperature at the beginning and then turns to an increasing trend after passing a critical temperature in the range of ~700–750 K. Meanwhile, the effect of temperature on ε_c is minimal. The theoretical analysis below is then intended to capture these observations in ε_c .

Microscopically, the kinetics of serrations is associated with the motion of dislocations and the hindrance from solutes. So does its dependence on the temperature and strain rate. Firstly, by considering the coupled dynamics of gliding dislocations and solutes along with the evolution of the flow stress, activation volume, and dislocation densities with strain, the plastic flow is thought to be-

S. Chen, W. Li, F. Meng et al. Scripta Materialia 200 (2021) 113919

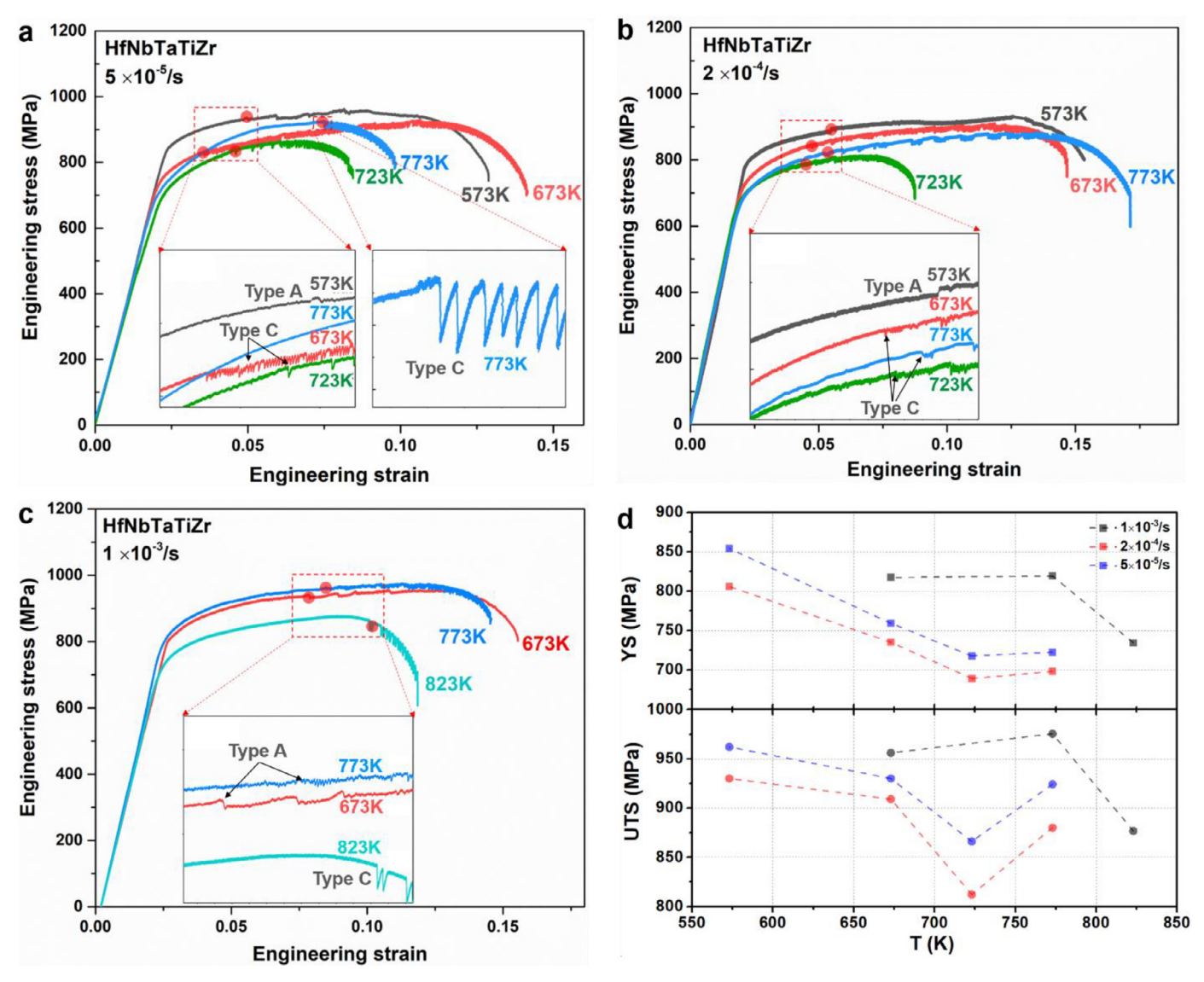


Fig. 2. Temperature dependence of the uniaxial tensile behavior of the HfNbTaTiZr alloy at the strain rate of (a) $5 \times 10^{-5} \text{ s}^{-1}$, (b) $2 \times 10^{-4} \text{ s}^{-1}$, and (c) $1 \times 10^{-3} \text{ s}^{-1}$. (d) Temperature dependence of yield strength (YS) and ultimate tensile strength (UTS) at three applied strain rates.

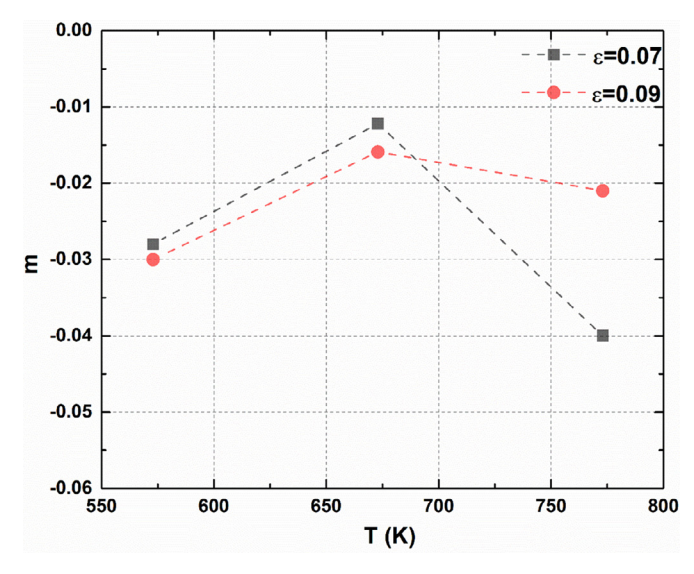


Fig. 3. Strain rate sensitivity (SRS) calculated at various temperatures and strain levels

Table 1YS, UTS, elongation at failure (EL), and critical strain, ε_c , at various testing temperatures and strain rates.

	T (11)	VC (NED)	LITTO (LED.)	Er	
Strain rate (s ⁻¹)	T (K)	YS (MPa)	UTS (MPa)	EL	ε_c
5×10^{-5}	573	854	962	0.128	0.049
	673	759	930	0.141	0.037
	723	717.5	866	0.084	0.046
	773	722.4	924	0.098	0.074
2×10^{-4}	573	805.7	930	0.15	0.054
	673	734.8	909	0.146	0.047
	723	689	812	0.087	0.037
	773	698	880	0.17	0.052
1×10^{-3}	673	817.4	956	0.15	0.078
	773	819.1	975.3	0.145	0.083
	823	734.3	876.6	0.118	0.1

$$S < -(\theta - \tau^{ext})\dot{\gamma}t_{DSA} \tag{2}$$

where $S = \frac{\partial \tau^{ext}}{\partial ln\dot{\gamma}}$ is the strain-rate sensitivity, $\theta = \frac{\partial \tau^{ext}}{\partial \gamma}$ the strain-hardening coefficient, τ^{ext} the flow stress, $\dot{\gamma}$ the applied strain rate, and t_{DSA} the characteristic DSA time scale.

S. Chen, W. Li, F. Meng et al. Scripta Materialia 200 (2021) 113919

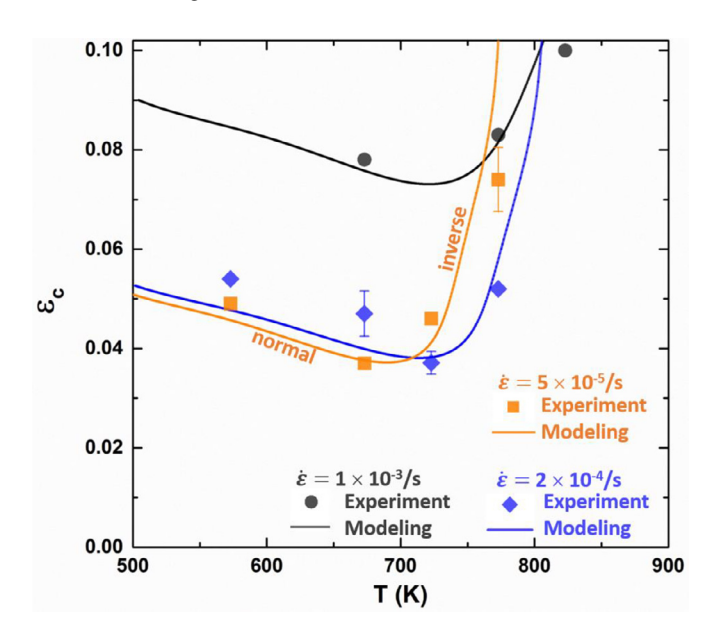


Fig. 4. The variation of the critical serration strain, γ_c (or ε_c), with temperatures and strain rates predicted from numerically solving Eqs. (7) – (9) (solid lines) along-side experimental data (symbols).

With an Arrhenius law for the stress-assisted thermal activation process, the strain-rate sensitivity is given as

$$S = S_0 - n \frac{\Delta G}{V} \left(\frac{\eta \Omega}{\dot{\gamma}} \right)^n exp \left[-\left(\frac{\eta \Omega}{\dot{\gamma}} \right)^n \right]$$
 (3)

$$S_0 = \frac{k_B T}{V} \tag{4}$$

where n is the characteristic aging exponent depending on strengthening mechanisms and diffusion modes. ΔG denotes the maximum increase of the free activation enthalpy as a result of the DSA process. V represents the activation volume. η is the characteristic rate of DSA in proportion to the solute mobility. Ω is the elementary strain accomplished as all mobile dislocations have undergone a thermal activation event. k_B is the Boltzmann constant, and T is temperature.

With the proper considerations of the statistics of DSA [19,20], t_{DSA} is derived as

$$t_{DSA} = \eta \frac{\Delta G}{k_{B}T} \frac{\frac{\dot{\gamma}}{\Omega}}{\left(\frac{\dot{\gamma}}{\Omega} + \eta\right)^{3}}$$
 (5)

For the case of weak aging, setting n = 1 [19,20] and combining Eqs. (2)–(5), the plastic-flow instability criterion reads as

$$exp\left[-\frac{\eta\Omega}{\dot{\gamma}}\right] > \frac{\left(\theta - \tau^{ext}\right)V\Omega}{k_BT} \frac{\dot{\gamma}^3}{\left(\dot{\gamma} + \eta\Omega\right)^3} + \frac{k_BT}{\Delta G} \frac{\dot{\gamma}}{\eta\Omega} \tag{6}$$

With the necessary dimensional analysis, Eq. (6) is reduced to

$$B < B_c(X, Y) = (1+X)^3 \left[\exp(-X) - \frac{Y}{X} \right]$$
 (7)

where $X=\frac{\eta\Omega}{\dot{\gamma}}$ represents the scaled aging time. $Y=\frac{k_BT}{\Delta G}$ is the reciprocal capacity for DSA. $B=\frac{(\theta-\tau^{\rm ext})V\Omega}{k_BT}$ denotes the dimensionless effective strain-hardening coefficient.

Assuming a linear hardening rule based on our measurement data in Fig. 2a-c, i.e., $\tau^{ext}=\tau_0+\theta\gamma$ with θ being a constant, $B(\tau^{ext})$ can be transformed into $B(\gamma)$. Specifically, letting $X(\gamma)=X^*+\frac{\eta\Omega'}{\gamma}\gamma$ with $X^*=\frac{\eta\Omega^*}{\gamma}$ and $\Omega'=\partial\Omega/\partial\gamma$, it reaches

$$B(X) = B^* - \frac{m}{Y^*}(X - X^*)$$
(8)

Table 2Material parameters and values used in Eq. (7) – (9) for producing theoretical trajectories of the critical serration strains with varied temperatures and strain rates in Fig. 4.

Strain rate (s ⁻¹)	G_s (eV)	Y	Α	m	B*	Ω^*	Ω'
$\begin{array}{c} 1 \times 10^{-3} \\ 2 \times 10^{-4} \\ 5 \times 10^{-5} \end{array}$	0.5	0.05	1.8	0.20	15	0.05	41
	0.5	0.05	1.8	0.195	10	0.09	84.6
	0.5	0.05	1.8	0.19	9.8	0.12	115.2

with $B^* = \frac{(\theta - \tau_0)V^*\Omega^*}{k_BT}$ and $m = \frac{V^*(\Omega^*)^2\theta}{k_BT\Omega'}$, where all parameters in the form of ()* represents constants.

The critical condition for the onset of serrations in terms of X at different values of X^* can be determined by numerically solving the non-linear equation $B(X) = B_c(X)$, i.e., equating Eqs. (7) and (8). By noting that $X(\gamma) = X^* + \frac{\eta \Omega'}{\dot{\gamma}} \gamma$, $X^* = \frac{\eta \Omega^*}{\dot{\gamma}}$, the critical condition can be readily transformed from the $\{X^*, X\}$ space back into the $\{\dot{\gamma}, \dot{\gamma}\}$ space, thereby obtaining the critical serration strain, the strain at which a serration initiates, at different strain rates.

The temperature effect on the critical serration strain can be considered as well by noticing that the solute mobility scales with the temperature as [19]

$$\eta = Aexp\left(\frac{-G_s}{k_P T}\right) \tag{9}$$

where G_s is the free enthalpy of solute diffusion, and A is a constant. Likewise, with Eq. (9), the critical condition can be transformed from the $\{X^*, X\}$ space into the $\{T, \gamma\}$ space. The temperature effect on the critical serration strain can therefore be quantified.

Using the theoretical framework described above, the variation of the critical serration strain, γ_c , with temperatures and three strain rates applied in the measurements (i.e., 5×10^{-5} , 2×10^{-4} , and $1 \times 10^{-3} \text{ s}^{-1}$) is predicted and plotted in Fig 4. The corresponding values of material parameters are listed in Table 2, in which G_s , Y, and A are assumed to be independent of strain rates. Alongside shown as symbols in Fig. 4 are the experimental data extracted at available temperatures (573-823 K) and strain rates. Overall, the theoretical predictions agree well with experimental data, and successfully capture the effect of temperatures and strain rates on the critical serration strain. The temperature effect firstly exhibits a "normal behavior" (i.e., the onset of the serrated flow increases with decreasing temperature), and transitions to an "inverse behavior" (i.e., the onset of the serrated flow increases with increasing temperature) at a given temperature. This transition temperature is predicted to be 691.85, 720.85, 729.85 K respectively for the strain rate of 5 \times 10⁻⁵, 2 \times 10⁻⁴, and 1 \times 10⁻³ s⁻¹, manifesting an upward trend with rising strain rate. The strain rate effect, on the other hand, shows a "normal behavior", i.e., the onset of the serrated flow increases with increasing strain rate.

The normal behavior at low temperatures is common in many dilute solid solutions [18,21–23]. The critical strain of such normal behaviors depends on the pinning state of the mobile dislocations by solutes [24]. On the other hand, the inverse behavior that occurs at high temperatures is less common in dilute solid solutions, but mostly observed in concentrated solid solutions like HEAS [9,25,26]. The previously-reported inverse behavior induced by precipitate dissolution and reprecipitation is deemed unlikely in the present work, as the BCC structure of the alloy remain stable without the formation of any second phases, which is affirmed by Synchrotron diffractions (not shown). Thus, the inverse behavior is argued to be controlled by the diffusion kinetics associated with DSA [18,24]. Such serration behavior is also observed in other HEAS, such as the CoCrFeMnNi [13] and Al_xCoCrFeNi [8–12].

In summary, when uniaxially tensioning the HfNbTaTiZr HEA at temperatures of 573–823 K and strain rates of 5 \times $10^{-5}\ s^{-1}$

 -1×10^{-3} s⁻¹, flow serration is noticed in all conditions. Temperature and strain rate tend to alter not only the strength and stress-strain curve shape of the alloy, but also the flow-serration type and the onset strain of the serrated flow, ε_c . In particular, pronounced temperature dependence of ε_c is observed, in spite of its negligible change with strain rates. The normal (i.e., ε_c decreases with temperature) and inverse (i.e., ε_c increases with temperature) behaviors of ε_c with varying temperatures at different strain rates are neatly captured with a theoretical model. The model is useful for defining the process window when coming to manufacturing or processing the HfNbTaTiZr HEA. The model outlined herein is also readily expandable to other HEA systems.

Declaration of Competing Interest

There are no conflicts of interest to declare.

Acknowledgement

S. C. acknowledges the financial support from the National Natural Science Foundation of China (No. 52001271). Y.T. acknowledges the financial support programs, Taishan Scholars Youth Expert Program. P. K. L. very much appreciates the supports from (1) the National Science Foundation (DMR-1611180 and 1809640) with program directors, Drs. J. Yang, G. Shiflet, and D. Farkas and (2) the US Army Research Office (W911NF-13-1-0438 and W911NF-19-2-0049) with program managers, Drs. M.P. Bakas, S.N. Mathaudhu, and D.M. Stepp. This work was financially supported by the "High Entropy Materials Center" from The Featured Areas Research Center Program within the framework of the Higher Education Sprout Project by the Ministry of Education (MOE) and from the Project MOST 109-2634-F-007-024 - by Ministry of Science and Technology (MOST) in Taiwan. Z. G. W. acknowledges the financial support from National Natural Science Foundation of China (No. 51901077). This research used resources of the Advanced Photon Source, a U.S. Department of Energy (DOE) Office of Science User Facility, operated for the DOE Office of Science by Argonne National Laboratory under Contract No. DE-AC02-06CH11357.

References

- [1] P.G. McCormick, Acta Metal. 19 (5) (1971) 463-471.
- [2] J. Brechtl, S. Chen, C. Lee, Y. Shi, R. Feng, X. Xie, D. Hamblin, A.M. Coleman, B. Straka, H. Shortt, R. J. Spurling, P.K. Liaw, Metals 10 (8) (2020) 1101.
- [3] J. Brechtl, S.Y. Chen, X. Xie, Y. Ren, J.W. Qiao, P.K. Liaw, S.J. Zinkle, Int. J. Plast. 115 (2019) 71-92.
- [4] Y. Zhang, J.P. Liu, S.Y. Chen, X. Xie, P.K. Liaw, K.A. Dahmen, J.W. Qiao, Y.L. Wang, Prog. Mater. Sci. 90 (2017) 358-460.
- [5] P. Rodriguez, Bull. Mater. Sci. 6 (4) (1984) 653-663.
- [6] W. Li, D. Xie, D. Li, Y. Zhang, Y. Gao, P.K Liaw, Prog. Mater. Sci. (2021) 100777.
- [7] W. Li, S. Chen, P.K. Liaw, Scripta Mater. 187 (2020) 68–75. [8] S. Chen, X. Xie, W. Li, R. Feng, B. Chen, J. Qiao, Y. Ren, Y. Zhang, K.A. Dahmen, P.K. Liaw, Mater. Chem. Phys. 210 (2018) 20-28.
- [9] T. Yang, Z. Tang, X. Xie, R. Carroll, G. Wang, Y. Wang, K.A. Dahmen, P.K. Liaw, Y. Zhang, Mater. Sci. Eng. A (2017) 552-558.
- [10] H.Y. Yasuda, K. Shigeno, T. Nagase, Scripta Mater. 108 (2015) 80-83.
- [11] J. Joseph, P. Hodgson, T. Jarvis, X. Wu, N. Stanford, D.M. Fabijanic, Mater. Sci. Eng. A 733 (2018) 59-70
- [12] Y. Zhang, J. Li, J. Wang, W.Y. Wang, H. Kou, E. Beaugnon, J. Alloys Compd. 757 (2018) 39-43.
- [13] R. Carroll, C. Lee, C.W. Tsai, J.W. Yeh, J. Antonaglia, B.A. Brinkman, M. LeBlanc, X. Xie, S. Chen, P.K. Liaw, K.A. Dahmen, Sci. Rep. 5 (2015) 16997.
- [14] S.F. Ge, Mater. Sci. Eng. A 784 (2020) 139275.
- [15] W.A. Curtin, D.L. Olmsted, L.G. Hector Ir, Nat. Mater. 5 (2006) 875-880.
- [16] F. Zhang, W.A. Curtin, Modeling Simul. Mater. Sci. Eng. 16 (2008) 055006.[17] S.Y. Chen, L. Wang, W.D. Li, Y. Tong, K.K. Tseng, C.W. Tsai, J.W. Yeh, Y. Ren, W. Guo, J.D. Poplawsky, P.K. Liaw, Mater. Res. Lett. 7 (12) (2019) 475-481.
- [18] K. Gopinath, A.K. Gogia, S.V. Kamat, U. Ramamurty, Acta Mater. 57 (4) (2009) 1243-1253.
- [19] P. Hähner, Acta Mater. 45 (1997) 3695-3707.
- [20] P. Hähner, Mater. Sci. Eng. A 207 (1996) 208–215.
- [21] L. Ziani, S. Boudrahem, H. Ait-Amokhtar, M. Mehenni, B. Kedjar, Mater. Sci. Eng. A 536 (2012) 239-243.
- [22] A. Chatterjee, G. Sharma, R. Tewari, J.K. Chakravartty, Metall. Mater. Trans. A 46 (3) (2014) 1097-1107.
- [23] F.F. Han, B.M. Zhou, H.F. Huang, B. Leng, Y.L. Lu, J.S. Dong, Z.J. Li, X.T. Zhou, Mater. Chem. Phys. (2016).
- [24] S. Fu, T. Cheng, Q. Zhang, Q. Hu, P. Cao, Acta Mater. 60 (2012) 6650–6656.
- [25] Y. Brechet, Y. Estrin, Acta Metall. Mater. 43 (3) (1995) 955-963.
- [26] C.-W. Tsai, C. Lee, P.-T Lin, X. Xie, S. Chen, R. Carroll, M. LeBlanc, B.A.W. Brinkman, P.K. Liaw, K.A. Dahmen, J.-W. Yeh, Int. J. Plast. 122 (2019) 212-224.